Chemical Science

rsc.li/chemical-science

Volume 9
Number 1
7 January 2018
Pages 1-268

ISSN 2041-6539

ROYAL SOCIETY
OF CHEMISTRY

EDGE ARTICLE
Xinjing Tang et al.
Caged circular siRNAs for photomodulation of gene
expression in cells and mice

ROYAL SOCIETY
OF CHEMISTRY

rsc.li/chemical-science

ARTICLE

Dynamic Surface Reconstruction Engineers Interfacial Water Structure for Efficient Alkaline Hydrogen Oxidation

Chaoyi Yang, Zihao Dai, Jianchao Yue, Guangqin Wang, and Wei Luo*

Investigating the dynamic evolution of the catalyst and regulating the structure of interfacial water molecules on hydrogen oxidation reaction (HOR) are essential for developing highly efficient electrocatalysts toward the practical application of anion exchange membrane fuel cells. Herein, we report an efficient strategy to active hexagonal close-packed PtSe catalyst through *in situ* reconstruction, undergoing dynamic Se leaching and phase transition during the linear sweep voltammetry cycles. The obtained Pt-Se catalyst with surface Se atoms modified face-centered-cubic Pt-based nanocatalyst exhibits remarkable catalytic performance toward alkaline HOR, showing the intrinsic activities of 0.552 mA cm^{-2} ($j^{0,s}$) and mass activities of 1.084 mA μg^{-1} ($j^{k,m}$ @ 50 mV). Experimental results including *in situ* surface-enhanced infrared absorption spectroscopy and the density functional theory calculations suggest that the accumulated electrons on the surface-decorated Se of Pt-Se can induce the regulation of interfacial water structure between the electrode and electrolyte surface in the electric double layer region. Consequently, the migration of OH$^-$ species from the electrolyte to the catalyst surface can be apparently accelerated within this disordered water network, which together with the optimized intermediate thermodynamic binding behaviors, contributes to the enhanced alkaline HOR activity.

Introduction

For the future environmental-friendly energy demands, the hydrogen fuel cell is one of the most promising candidates for the replacement of fossil fuels.[1-2] Anion exchange membrane fuel cell (AEMFC) has been recognized as the competitive energy conversion device owing to its merits of high energy density, zero carbon emission and sustainability.[3-5] Different from the well-developed cathodic oxygen reduction reaction (ORR) within the precious metal-free catalysts under alkaline media, severe dependence on the high loading noble-price-metal catalysts of alkaline anode hydrogen oxidation reaction (HOR) greatly hinder the practical application of the AEMFC.[6-8] Recently, the dynamic evolution of catalysts has been recognized during the electrocatalysis and the effects of pre-catalyst-reconstruction in various electrochemical catalytic processes, including oxygen evolution reaction,[9-11] carbon dioxide reduction reaction,[12-14] nitrate reduction reaction,[15-16] and hydrogen evolution reaction[17-18] have been widely investigated. The reconstructed structure and the redistribution of elements during the dynamic evolution can lead to the boosting of the catalytic activity, which are benefit for the design of advanced electrocatalysts.[19-20] Unfortunately, identifying the dynamic evolution process and activating the catalytic performance through reconstruction are essential for the rational design of advanced HOR electrocatalysts under alkaline electrolyte, but have been rarely investigated.

College of Chemistry and Molecular Sciences, Wuhan University, Wuhan, Hubei 430072, P. R. China. Email: wluo@whu.edu.cn

Recently, during the alkaline HOR process, the OH species engaged in the Volmer step, knowing as the rate determined step, has received considerable attentions.[21-22] Through the advanced spectroscopy technology, the adsorbed OH species has been detected during the alkaline HOR process by Li et al., directly demonstrating the involvement of OH$_{ad}$.[23] Markovic et al. proved that the metal with improved hydroxyl adsorption may present much higher alkaline HOR activities,[24] guiding the direction for rational designing highly efficient alkaline HOR electrocatalysts. Consequently, plenty of studies mainly focus on the thermodynamics energetics of OH$_{ad}$, which can dictate the catalytic activity derived from the charge redistribution and electronic adjustment-induced adsorption behavior modulation.[25-27] Besides, there is a growing recognition that the catalytic performance does not solely depend on the inherent structures of catalysts, but is also shaped by the electrochemical interface and the electric-double-layer (EDL) structure formed at the interface between the electrode and electrolyte.[28] However, owing to the decreased flexibility of interfacial water network in alkaline media, additional energy is needed for the migration of OH species from electrolyte to the catalyst surface, thereby leading to the sluggish HOR kinetics under alkaline electrolyte.[29-31] Therefore, rational regulating the interfacial water structure and decreasing the rigidity of water network to facilitate OH species across the EDL can be an efficient way to accelerated the alkaline HOR kinetic, but still remains challenging.

Herein, we proposed an efficient strategy through *in situ* reconstruction to boost the HOR performance of hexagonal close-packed (hcp) PtSe alloys under alkaline electrolytes. Compared with hcp-PtSe alloys with negligible catalytic
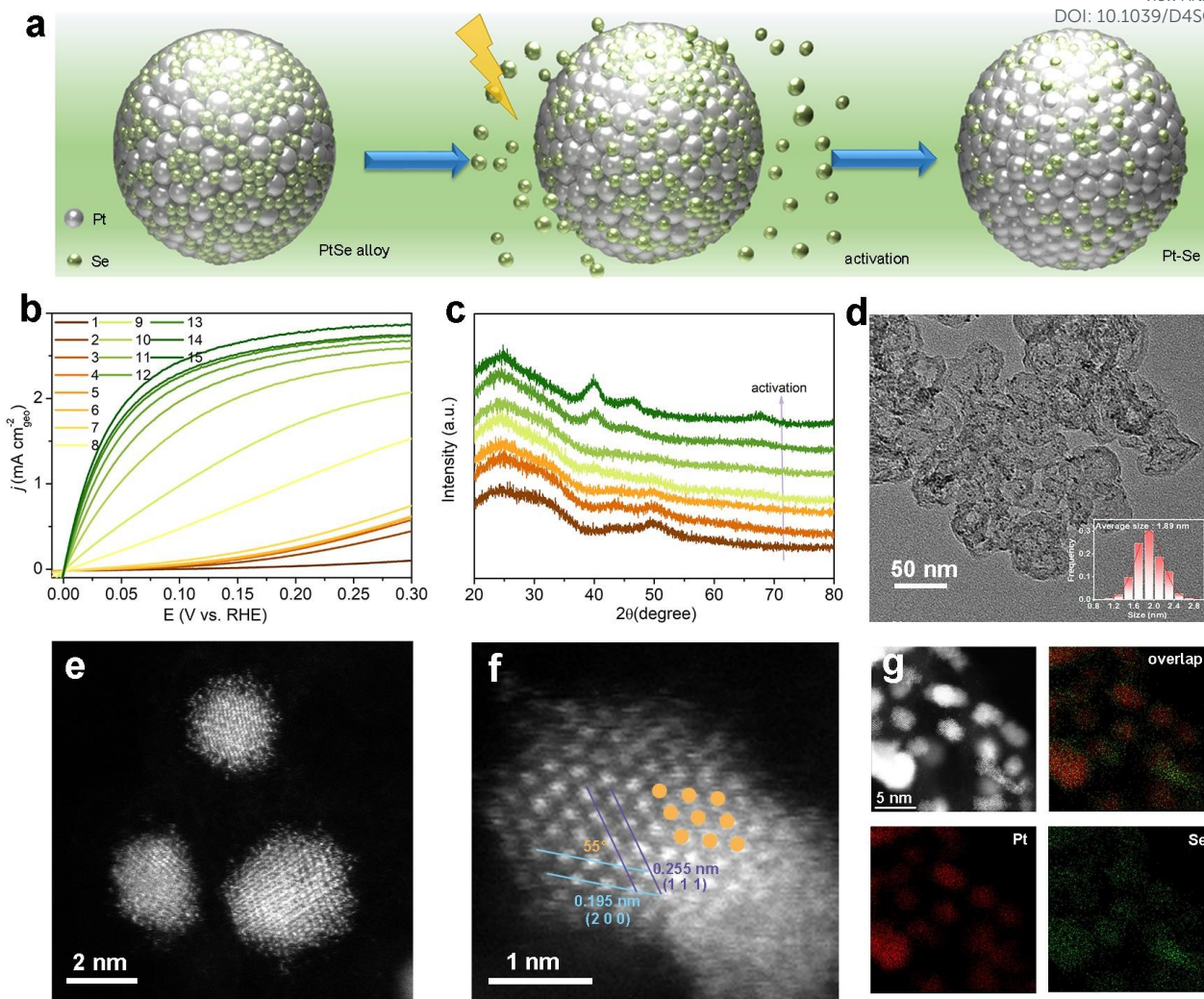
Fig. 1 (a) Schematic illustration for the activation process of the leaching of Se and phase transition on the PtSe alloy during the HOR process. The green balls present the Se atoms and the silver balls present the Pt atoms. (b) The activation process of PtSe$_2$ under the HOR polarization scans. (c) XRD patterns of PtSe$_2$ during the activation process. (d) Typical TEM image and the corresponding size distribution of Pt-Se-2. HAADF-STEM image (e) and atomic-resolution HAADF-STEM image (f) of Pt-Se-2. (g) HAADF-STEM image and corresponding EDX mappings of Pt-Se-2.

performance, face-centered-cubic (fcc) Pt-Se formed through the dynamic leaching of Se atoms and the follow-up phase transition during the electrocatalysis process displays significantly boosted HOR performance under alkaline electrolyte (Fig 1a), with the intrinsic activities of 0.552 mA cm^{-2} ($j^{0,s}$) and mass activities of 1.084 mA μg^{-1} ($j^{k,m}$ @ 50 mV). By the analyses of *in situ* surface-enhanced infrared absorption spectroscopy (SEIRAS) and the theoretical calculation, it is clear that the rigid water network on the interface of Pt-Se has been largely impaired through the regulation of the water structure by the inducing of the surface-decorated Se atoms, leading the facilitated migration of OH species to the catalyst surface, which together with the optimized intermediate adsorption, contributes to the enhanced alkaline HOR performance.

Results and discussion

The PtSe$_x$ alloys (x=1.5, 2, 3) with different Pt:Se ratio are successfully synthesized through colloid method (detailed experimental process is shown in supporting information) and the corresponding X-ray diffraction (XRD) in Fig. S1 are both depicted with the broad peak around 30 ° and 50 °, which can be assigned to the hexagonal close-packed structure. [32-33] The HOR performance of PtSe alloys are tested by rotating disk electrode (RDE) with 3-electrode system by using H$_2$-saturated 0.1 M KOH electrolyte. As shown in Fig. 1b and Fig. S2, the PtSe$_x$ present the gradually increased current densities during the linear sweep voltammetry (LSV) cycles and the HOR performances finally reach the steady state after several LSV sweeps, indicating the dynamic evolution of PtSe$_x$ during the HOR activation process. The activation processes for PtSe$_x$ also prolong with the increased content of Se. The stabilized catalysts after *in situ* reconstruction are noted as Pt-Se-x (x=1.5, 2, 3), while Pt-Se-2 presenting the highest alkaline HOR
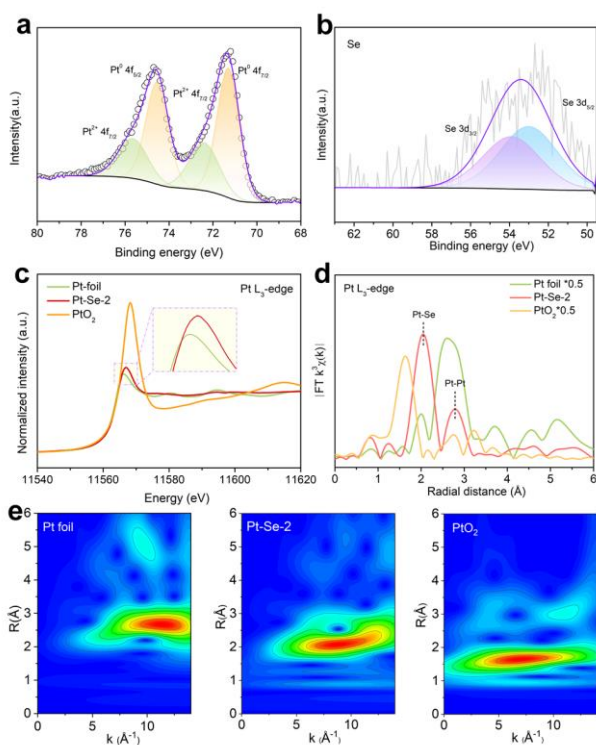
Fig. 2 XPS spectra of Pt 4f (a) and Se 3d (b) for Pt-Se-2. Pt L_3-edge XANES spectra (c) and corresponding FT-EXAFS spectrum spectra (d) of Pt-Se-2 in reference to Pt foil and PtO_2. (e) WT for the k^3-weighted EXAFS of the Pt L_3-edge for Pt-Se-2, Pt foil and PtO_2

performance among the three activated catalysts (*vide infra*). As the activation process proceeds, the cyclic voltammetry (CV) curves (Fig. S3) display a flat current in the hydrogen underpotential desorption region at the beginning, and then gradually show the underpotential desorption peaks of H (H_{upd}) on Pt, implying the exposure of Pt atoms and the potential phase transformation during the activation.[34-35] The XRD patterns (Fig. 1c) during the activation process clearly indicate that the crystalline phase of $PtSe_2$ gradually changes from the initial hcp phase to the fcc phase of Pt-Se-2, which is well matched with the standard Pt (PDF#89-7382). Different ratio of Pt-Se-x also show the same XRD patterns after the activation (Fig. S4). Furthermore, the precise composition of $PtSe_2$ alloy and activated Pt-Se-2 are both collected by the inductively coupled plasma atomic emission spectroscopy (ICP-AES) in Table S1. It is clear that the content of Se is significantly decreased after the activation, indicating that the majority of Se atoms are leaching during the activation and only part of them can stabilized in the final catalyst. As the amount of Se feed grows, the ratio of the stabilized Se on catalysts is enhanced as well. Through the transmission electron microscopy (TEM) in Fig. 1d, the morphology of Pt-Se-2 shows the small nanoparticles uniformly distributed on the XC-72R carbon with the average size of 1.89 nm. In the TEM image of $PtSe_2$, it also presents the evenly distributed small nanoparticles on the substitute, implying the little influence of activation on morphology (Fig. S5). To further investigate the structure of the activated catalyst and identify the existence form of Se after the activation, the high-angle annular dark-field scanning TEM (HAADF-STEM) is

employed. In Fig. S6, the HAADF-STEM image of $PtSe_2$ alloy presents the hexagonal packed of the atoms, which is in line with the results of XRD. The Pt and Se elements spread evenly on the nanoparticles through the energy-dispersive X-ray (EDX, Fig. S7). The HAADF-STEM image of Pt-Se-2 demonstrates that the inner part of the nanoparticle presents apparently crystallinity while the outside shows the obvious amorphous atomic layers (Fig. 1e). As shown in Fig. 1f, the atomic-resolved lattice spacings of the inner part of Pt-Se-2 are measured to be 0.195 nm and 0.225 nm, attributed to the (200) facet and (111) facet of fcc Pt, respectively. The angle between the (200) and (111) planes is 55°, which further indicating the face-centered-cubic phase. The corresponding fast Fourier transform (FFT) of STEM image in Fig. S8 also shows the crystal lattice orientated is based on the [011] crystallographic direction of fcc Pt, which is in line with the XRD pattern. The energy-dispersive X-ray (EDX) mappings (Fig. 1g) and the line scan signals (Fig. S9) both present that the remaining Se atoms prefer to stabilize on the surface around the crystalline phase. In addition, the surface elements content of Pt-Se-2 is also conducted by XPS in Table S2. Comparing with the Se/Pt ratio in the bulk of Pt-Se-2 obtained by ICP-AES, higher atomic ratio of Se/Pt conducted by XPS further confirms the surface decorating of Se atoms in Pt-Se-2.

The X-ray photoelectron spectroscopy (XPS) was applied to probe the electronic states of Pt and Se in Pt-Se-2. The high-resolution XPS spectra of Pt 4f (Fig. 2a) can be deconvolved into four peaks, corresponding to the Pt^0 $4f_{7/2}$, Pt^0 $4f_{5/2}$ electrons at 71.3 eV and 74.6 eV and Pt^{2+} $4f_{7/2}$, Pt^{2+} $4f_{5/2}$ electrons at 72.4 eV and 75.7 eV, respectively.[36] The valence state of Pt in Pt-Se-2 is slightly higher than that of Pt (Fig. S10), indicating the electron transfer from Pt to Se atoms. Comparing with the $PtSe_2$ alloy (Fig. S11), the peak position of Pt for Pt-Se-2 is slightly shift to the lower binding energies, which may contribute to the decrease content of Se. In addition, the Se 3d spectrum (Fig. 2b) shows the peaks located at 52.5 eV and 53.4 eV, which can be assigned to the $3d_{5/2}$ and $3d_{3/2}$ of selenide, respectively. Comparing with the Se powder (Fig. S12), the down shift of the valence state further proves the electron transfer process in Pt-Se-2. Specifically, no obvious peak located around 59 eV can be observed, implying that no selenates existed on the surface.[37-38] Considering the relative low potential of HOR process, the Se atoms were merely leaching and did not oxidize on the surface during the LSV scans, leading the Se atoms in Pt-Se-2 still keeps the zero-valence state after the activation, same with that before activation (Fig. S11). Besides, the X-ray adsorption spectroscopy (XAS) in Pt L_3-edge was performed to further achieve the electronic state on the Pt-Se-2. As shown in Fig. 2c, the Pt L_3-edge X-ray adsorption near edge structure (XANES) of Pt-Se-2 shows the relatively low intensity of white line close to that of Pt foil, revealing the metallic state of Pt in Pt-Se-2 and the slight electron loss on Pt in line in with the XPS results. The Fourier-transformed extended X-ray absorption fine structure (FT-EXAFS) spectra (Fig. 2d) and the Wavelet transforms (WT) for k^3-wieghted EXAFS signals (Fig. 2e) of Pt L_3-edge both confirm the existence of Pt-Se bond and Pt-Pt and the lack of Pt-

ARTICLE
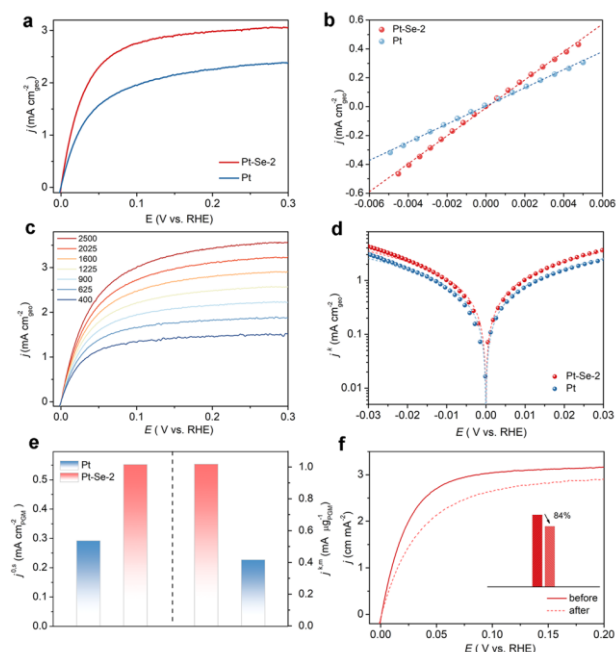
Fig. 3 (a) The HOR polarization curves of Pt-Se-2 and commercial Pt at the rotating speed of 1600 rpm with a scan rate of 10 mV s^{-1} in H_2-saturated 0.1 M KOH. (b) Linear-fitting curves in the micro-polarization region of HOR polarization curves of Pt-Se-2 and commercial Pt. (c) Polarization curves of Pt-Se-2 in H_2-saturated 0.1 M KOH electrolyte at the rotating speeds varied from 2500 to 400 rpm. (d) Tafel plots with the Butler–Volmer fitting lines of Pt-Se-2 and commercial Pt. (e) Comparison of the specific activities($j^{0,s}$) and the mass activities ($j^{k,m}$)(@ 50 mV) of Pt-Se-2 and commercial Pt. (f) HOR polarization curves of Pt-Se-2 in H_2-saturated 0.1 M KOH at a rotating speed of 1600 rpm before and after 1000 CVs.

O bond, further reveal the Pt atoms are not oxidized during the activation process.

The HOR activities of Pt-Se-x samples were evaluated by the LSV in the fresh 0.1 M KOH electrolyte as shown in Fig. S13. Calculating the linear fitting of micropolarization regions from -5 to 5 mV through the simplified Butler–Volmer equation (Fig. S14), the exchange current density (j^0) normalized by the geometric area of the glassy carbon electrode (GCE) can be obtained.[39-40] With the increase of content of Se, the exchange current density (j^0) of Pt-Se-x increase at the first and then decline, indicating the existence of the optimized Se content for the HOR performance. Fig. S15 shows the LSV curves of Pt-Se-x at the rotation rates from 2500 to 400 rpm and the corresponding fitting of the Koutecky-Levich plots.[41] Calculating by the Butler-Volmer equation, the Tafel plots of kinetic current densities (j^k) can be obtained in Fig. S16, still presenting the same tendency as j^0. The mass activities ($j^{k,m}$) which is normalized by the mass of the Pt content obtained from the ICP-AES results (Fig. S17) show the same volcano correlation, confirming the Pt-Se-2 possesses the highest mass activity at 50 mV among the three catalysts. Through Cu underpotential deposition (Cu-UPD) stripping, electrochemical surface areas (ECSAs) were procured to further evaluate the intrinsic activities ($j^{0,s}$) of Pt-Se-x (Fig. S18). After normalized the exchange current density (j^0) by the ECSA, the Pt-Se-2 still shows much higher intrinsic activities ($j^{0,s}$) comparing with Pt-Se-1 and Pt-Se-3 (Fig. S17).

To further estimate the HOR performance of Pt-Se-2, the commercial Pt is considered for comparison. With the LSV curves of Pt and Pt-Se-2 in Fig. 3a, the exchange current density (j^0) calculated by the micropolarization regions (Fig. 3b) of Pt-Se-2 is apparently higher than that of commercial Pt. The different rotating rates of LSV curves of Pt-Se-2 and Pt are collected in Fig. 3c and Fig. S19. The kinetic current densities (j^k) of Pt-Se-2 reaches 7.13 mA cm^{-2} at 50 mV, exceeding the 4.24 mA cm^{-2} of Pt (Fig. 3d). Besides, the calculated mass activities ($j^{k,m}$) of Pt-Se-2 also presents as 1.084 mA μg^{-1} at 50 mV (Fig. 3e), which is over two times higher than that of commercial Pt (0.416 mA μg^{-1}). After normalized the ECSA by Cu stripping, the Pt-Se-2 displays remarkable intrinsic activities ($j^{0,s}$) of 0.552 mA cm^{-2}, showing 2-fold improvement compared with commercial Pt (0.292 mA cm^{-2}) (Fig. 3e and Fig. S20). Remarkably, the intrinsic activities ($j^{0,s}$) and mass activity of Pt-Se-2($j^{k,m}$)(@ 50 mV) exceed those of most noble metal-based HOR catalysts reported in previous studies (Table S3). The stability of Pt-Se-2 was also evaluated through the accelerated degradation test (ADT).[42] As depicted in Fig. 3f, the Pt-Se-2 maintains more than 80% of current density after the 1000 cycles, while the commercial Pt presents almost 40% decay of the HOR activity (Fig. S21), implying the significantly improvement of stability with the protection of surface-modified Se. After the stability test, the Pt-Se-2 still maintains the previous crystalline phase (Fig. S22), morphology (Fig. S23), nanoparticle size (Fig. S24) and chemical states (Fig. S25). Considering that the natural gas reforming is still the most widely used method for the production of H_2, the inevitable CO in H_2 which may poison the active sites during the HOR process leads the anti-CO property become the desirable characteristic for HOR catalysts. To evaluate the CO tolerance of the catalysts, the long-term electrocatalysis in CO-containing (100 ppm) H_2 saturated 0.1 M KOH was tested to poison the catalysts. As shown in Fig. S26, commercial Pt only maintains the 64.9% HOR performance after the CO poisoning, while the Pt-Se-2 can keep 79.3% activity comparing with that before the CO poisoning, suggesting the improved CO tolerance on Pt-Se-2.

In situ surface-enhanced infrared absorption spectroscopy (SEIRAS) within the potential range from 0 V to 0.2 V has been applied to investigate the interfacial water structure of the catalysts. As shown in Fig. 4a and 4b, the bands from 3000 to 3600 cm^{-1} are contributed to the O-H stretching mode of interfacial water, and can be deconvoluted into three distinct components. Specifically, the bands located near 3200 cm^{-1} can be assigned to the tetrahedrally coordinated H-bond water (i.e. ice-like water); the higher bands around 3400 cm^{-1} belong to the trihedarlly coordinated H-bond water (i.e. liquid-like water); the highest bands positioned at 3600 cm^{-1} can be attributed to weak-bond water (i.e. free water).[43-45] It is clear that the ice-like water nearly takes half proportion among the three components on Pt, implying the interfacial water structure on the surface of Pt is rigid with the strong hydrogen bonding (Fig. 4c).[31,46] This rigid water structure may lead to the much higher energy barrier for the reorganization of interfacial water, hindering the H_2O^*/OH* transfer process (Fig. 4e).[30] Functioned as the electron acceptors, the surface decorated Se
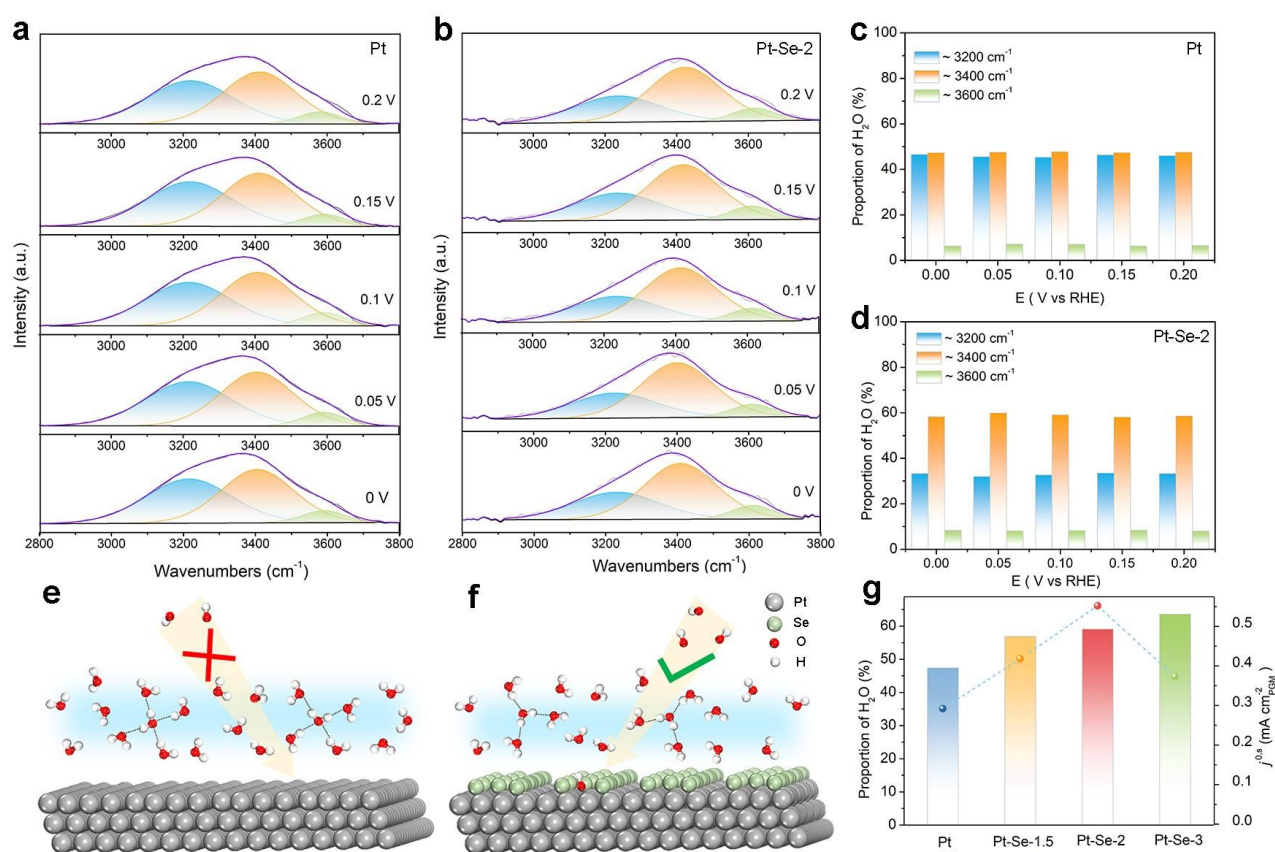
Fig. 4 Deconvolution of the O-H stretching vibration features of *in situ* SEIRAS spectra recorded at potentials from 0 V to 0.2 V vs RHE for Pt (a) and Pt-Se-2 (b) in 0.1 M KOH. The proportion of the three kinds of water molecules from the deconvolution of the O-H stretching vibration features of Pt (c) and Pt-Se-2 (d). The proposed mechanism for Pt (e) and Pt-Se-2 (f). The green balls present the Se atoms, the silver balls present the Pt atoms, the red balls present the O atoms and the white balls present H atoms. (g) The plots of the intrinsic activities ($j^{0,s}$) of alkaline HOR vs the proportion of the liquid- like water of Pt, Pt-Se-1.5, Pt-Se-2 and Pt-Se-3

on the Pt-Se-2 can be used to reorient the interfacial water molecules. [31,47-49] It is clear that on Pt-Se-2, the proportion of ice-like water apparently decreases while the proportion of the liquid-like water around 3400 cm^{-1} is significantly enhanced (Fig. 4d). Since this kind of asymmetric coordinate water is reported to be more flexible than the ice-like water, [44,50] the relatively disordered interfacial water network can be generated on the surface of Pt-Se-2, which can efficiently accelerate the H$_2$O*/OH* transport across the EDL, thereby leading to enhanced number of available OH species on the surface, and accelerated HOR kinetics in alkaline electrolyte (Fig. 4f).[31,50] Besides, it is also reported that comparing with the ice-like water, the water molecules located at higher frequencies is more sensitive to the local electric field and much closer to the surface, [50-51] which may lead the stronger electron interaction between water molecules and the surface of catalysts, accelerating the charge transfer and promoting the reaction at the same time. [43] The *in situ* SEIRAS of the catalysts with different content of Se were also collected in Fig. S27. As the increased amount of Se, the proportion of the ice-like water is decreased, indicating the strong water structure regulation of surface-decorated Se. However, the volcano relationship between HOR activity and the content of Se indicates that the

induced high content Se may lead to the decrease of the H donors and acceptors, and unfavorable HOR kinetics (Fig. 4g). [52-53]

The synergistic employment of density functional theory (DFT) calculations provides a deeper comprehension for the mechanism of Pt-Se-x in HOR process. The Se atoms binding on the hollow sites of Pt (111) facet is used as the model of Pt-Se-2 and the model of Pt with the (111) facet exposed also established for comparison (Fig. S28). As shown in Fig. 5a, the electrons of Pt on the surface tend to flow to the Se atoms, which consistent with the increase valence of Pt in the results of XPS, leading to electron accumulation on the Se site. According to the optimal theoretical structures of the H$_2$O adsorption on Pt and Pt-Se-2 (Fig. S29), it is clear that the H$_2$O molecule trends to transfer from O-down to parallel within the inducing of Se. [31,47,53] Electron localization function (ELF) evaluations are also employed for the excess kinetic energy density. [54] As shown in Fig. 5b, the strong binding of Pt-O result in this 'O-down' structure on the surface of Pt. Through the topological image in Fig. 5c, it is clear that the strong distribution of valence electrons in Se atoms leads to increased electron localization and formation of strong bond interaction with the O atoms of water molecules, testifying the structure
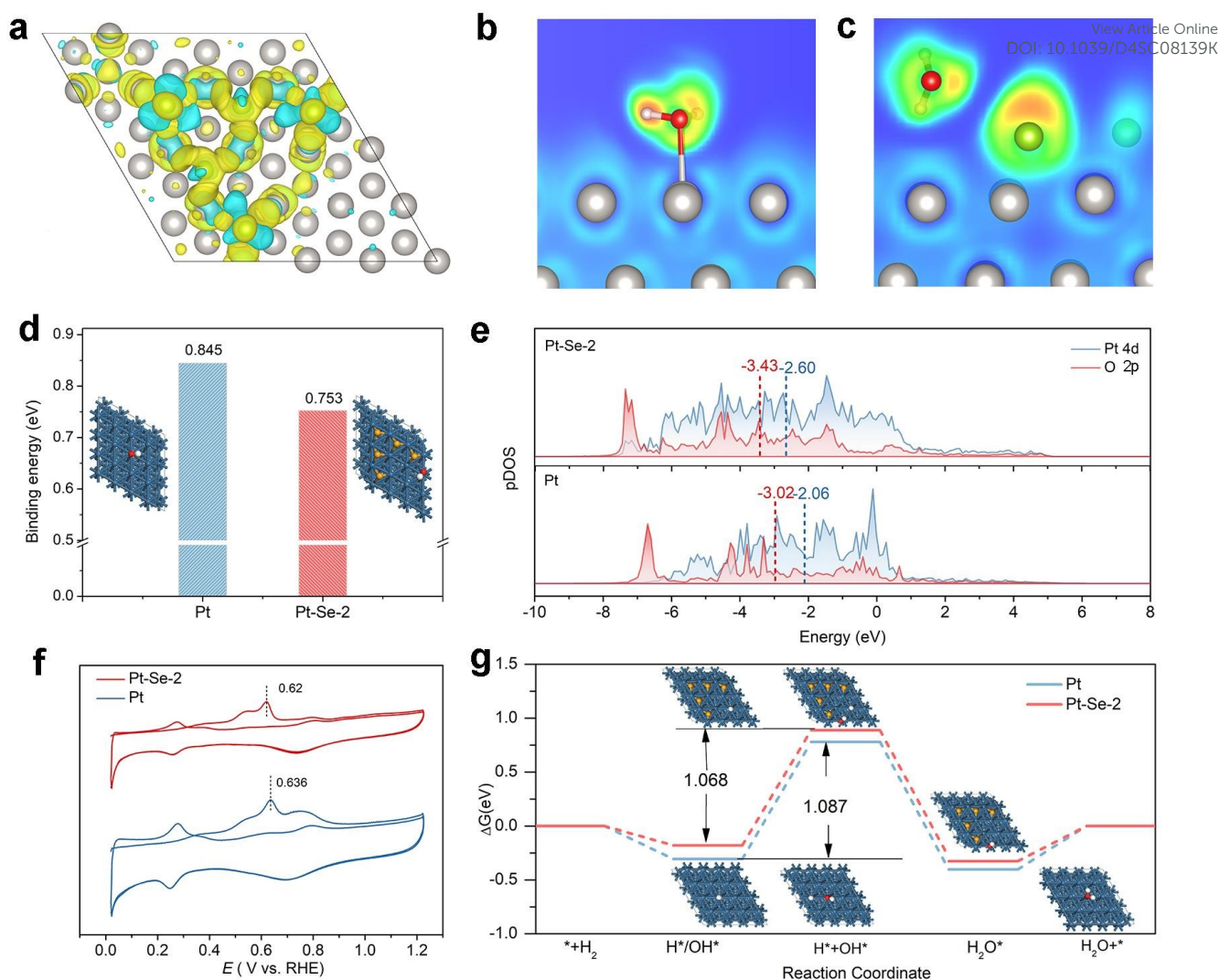
Fig. 5 (a) Calculated differential charge density for Pt-Se-2. ELF evaluation for H_2O adsorption on the Pt (b) and Pt-Se-2 (c). (d) The adsorption energy of OH*on Pt and Pt-Se-2 with the corresponding optimal theoretical structure. (e) The p-DOS of Pt 4d orbitals and O 2p orbitals in Pt and Pt-Se-2. (f) CO stripping curves of Pt and Pt-Se-2 in CO-statured 0.1 M KOH. (g) The reaction path of Pt and Pt-Se-2 and the corresponding optimized structure.

transform of interfacial water presented in the *in situ* SEIRAS. [54-56] Besides the transform of water structures, the adsorption energy can also be regulated through the electron redistribution owing to the introducing of Se. The OH binding energy of Pt-Se-2 clearly enhance comparing with that of Pt (Fig. 5d), which can also contribute to the improvement of HOR performance. According to the orbital coupling state diagram of Pt and Pt-Se-2 within the OH adsorption state (Fig. 5e), the electron cloud coincidence degree of Pt and O on Pt-Se-2 is obviously deeper than that of Pt, demonstrating increased filling of the bonding orbitals, and enhanced OH binding energy.[57-58] Furthermore, the apparently lowered CO-stripping peak of Pt-Se-2 in Fig. 5f comparing with Pt reveals the increasing OH adsorption within the introduction of Se, proving the conclusion of the calculation.[59-60] To further examine the relationship between the Se concentration and HOR performance, the modules with different amount of Se have been established to correspond to Pt-Se-1.5 and Pt-Se-3 (Fig.

S30). Similar to the water structure of Pt-Se-2, the water molecules also transfer to the parallel structure owing to the induce of the Se atoms on the surface (Fig. S31). Through the theoretical calculation in Fig. S32 and the CO stripping curves in Fig. S33, the OH binding energy of Pt-Se-x depicts the volcano correlation with the enhancement of Se, in line with the change of HOR performance. In addition, the adsorption of hydrogen atoms is taken into consideration (Fig. S34 and Fig. S35). Comparing with the Gibbs free energy of H (ΔG_H) on Pt, the ΔG_H of Pt-Se-x extremely decrease and the Pt-Se-2 demonstrates the ΔG_H closest to zero, greatly promoting the HOR performance as well.[61-62] Furthermore, the reaction path for the HOR process of Pt and Pt-Se-2 are calculated in Fig. 5g. The steps of adsorption of H*/OH* and the formation of water are both spontaneous for Pt and Pt-Se-2 while the water desorption step and the adsorption of H*+OH* is endothermic. Specially, the adsorption of H*+OH* for both Pt and Pt-Se-2 presents the highest energy barrier which can be considered as the rate determining step

(RDS). Owing to the enhanced adsorption of OH, decreased energy barrier is demonstrate on the Pt-Se-2, contributing to the promoted HOR process.

Conclusions

In summary, the HOR-inactive PtSe catalyst can be successfully activated though dynamic Se leaching and phase transition during the LSV cycles. The obtained Pt-Se-2 sample with surface Se atoms modified Pt-based nanocatalyst presents the elevated intrinsic activity of 0.552 mA cm^{-2}($j^{0,s}$) and mass activity of 1.084 mA µg^{-1}($j^{k,m}$ @ 50 mV), outperforming most of the reported catalysts toward alkaline HOR. Combining experimental results including *in situ* SEIRAS and DFT calculation, we reveal that the Se atoms on the surface can gather the electrons of the catalysts, and efficiently regulate the water structure, thereby leading to increased flexibility of the interfacial water network on Pt-Se surface, and facilitated migration of OH$^-$ species across the EDL to the surface of electrode, which together with the optimized thermodynamic adsorption, contributes to the enhanced alkaline HOR performance. Our work not only expands the horizon of the dynamic evolution of catalysts during the HOR process, but also provides a new strategy for the rational design of advanced electrocatalysts through interfacial water structure engineering toward HOR and beyond.

Author Contributions

CY, ZD, JY and GQ performed the material synthesis and electrochemical tests. CY performed the DFT calculations. WL supervised the work. CY and WL wrote the manuscript.

Conflicts of interest

There are no conflicts to declare.

Acknowledgements

Notes and references

1 M. H. Tang, S. M. Zhang and S. L. Chen, *Chem. Soc. Rev.*, 2022, **51**, 1529-1546.
2 M. Z. Jacobson, W. G. Colella and D. M. Golden, *Science*, 2005, **308**, 1901-1905.
3 Z. B. Cui, Z. H. Ren, C. Ma, B. W. Chen, G. Z. Chen, R. H. Lu, W. Zhu, T. Gan, Z. Y. Wang, Z. B. Zhuang and Y. H. Han, *Angew. Chem.-Int. Edit.*, 2024, **63**, e202404761.
4 W. Y. Ni, T. Wang, F. Héroguel, A. Krammer, S. Lee, A. Yao, A. Schüler, J. S. Luterbacher, Y. S. Yan and X. L. Hu, *Nat. Mater.*, 2022, **21**, 804-810.
5 L. C. Wei, N. Fang, F. Xue, S. H. Liu, W. H. Huang, C. W. Pao, Z. W. Hu, Y. Xu, H. B. Geng and X. Q. Huang, *Chem. Sci.*, 2024, **15**, 3928-3935.
6 W. Y. Ni, J. L. Meibom, N. Ul Hassan, M. Y. Chang, Y. C. Chu, A. Krammer, S. L. Sun, Y. W. Zheng, L. C. Bai, W. C. Ma, S. Lee, S. Jin, J. S. Luterbacher, A. Schüler, H. M. Chen, W. E. Mustain and X. L. Hu, *Nat. Catal.*, 2023, **6**, 773-783.
7 J. Zheng, W. C. Sheng, Z. B. Zhuang, B. J. Xu and Y. S. Yan, *Sci. Adv.*, 2016, **2**, e1501602.
8 S. L. Li, L. Shi, Y. J. Guo, J. Y. Wang, D. Liu and S. L. Zhao, *Chem. Sci.*, 2024, **15**, 11188-11228.
9 Y. R. Xue, J. J. Fang, X. D. Wang, Z. Y. Xu, Y. F. Zhang, Q. Q. Lv, M. Y. Liu, W. Zhu and Z. B. Zhuang, *Adv. Funct. Mater.*, 2021, **31**, 2101405.
10 S. W. Zuo, Z. P. Wu, G. K. Zhang, C. L. Chen, Y. F. Ren, Q. Liu, L. R. Zheng, J. Zhang, Y. Han and H. B. Zhang, *Angew. Chem. Int. Edit.*, 2024, **63**, e202316762.
11 S. L. Li, Z. C. Li, R. G. Ma, C. L. Gao, L. L. Liu, L. P. Hu, J. L. Zhu, T. M. Sun, Y. F. Tang, D. M. Liu and J. C. Wang, *Angew. Chem. Int. Edit.*, 2021, **60**, 3773-3780.
12 J. Q. Sang, P. F. Wei, T. F. Liu, H. F. Lv, X. M. Ni, D. F. Gao, J. W. Zhang, H. F. Li, Y. P. Zang, F. Yang, Z. Liu, G. X. Wang and X. H. Bao, *Angew. Chem. Int. Edit.*, 2022, **61**, e202114238.
13 R. Amirbeigiarab, J. Tian, A. Herzog, C. R. Qiu, A. Bergmann, B. R. Cuenya and O. M. Magnussen, *Nat. Catal.*, 2023, **6**, 837-846.
14 14. J. Y. Duan, T. Y. Liu, Y. H. Zhao, R. O. Yang, Y. Zhao, W. B. Wang, Y. W. Liu, H. Q. Li, Y. F. Li and T. Y. Zhai, *Nat. Commun.*, 2022, **13**, 2039.
15 J. Yang, H. F. Qi, A. Q. Li, X. Y. Liu, X. F. Yang, S. X. Zhang, Q. Zhao, Q. K. Jiang, Y. Su, L. L. Zhang, J. F. Li, Z. Q. Tian, W. Liu, A. Q. Wang and T. Zhang, *J. Am. Chem. Soc.*, 2022, **144**, 12062-12071.
16 F. Yang, P. Song, X. Ge, Y. Wang, T. Gunji, W. Zhang, X. Zhao and W. L. Xu, *Proc. Natl. Acad. Sci. U. S. A.*, 2023, **120**, e2301011120.
17 M. Li, H. Li, H. F. Fan, Q. F. Liu, Z. Yan, A. Q. Wang, B. Yang and E. R. Wang, *Nat. Commun.*, 2024, **15**, 6154.
18 Y. D. Pan, J. K. Gao, E. J. Lv, T. T. Li, H. Xu, L. Sun, A. Nairan and Q. C. Zhang, *Adv. Funct. Mater.*, 2023, **33**, 2303833.
19 J. X. Feng, X. S. Wang and H. Pan, *Adv. Mater.*, 2024, 2411688.
20 C. Xie, W. Chen, Y. Y. Wang, Y. H. Yang and S. Y. Wang, *Chem. Soc. Rev.*, 2024, 10852.
21 J. Durst, A. Siebel, C. Simon, F. Hasché, J. Herranz and H. A. Gasteiger, *Energy Environ. Sci.*, 2014, **7**, 2255-2260.
22 Y. K. Feng, S. G. Lu, L. H. Fu, F. L. Yang and L. G. Feng, *Chem. Sci.*, 2024, **15**, 2123-2132.
23 Y. H. Wang, X. T. Wang, H. J. Ze, X. G. Zhang, P. M. Radjenovic, Y. J. Zhang, J. C. Dong, Z. Q. Tian and J. F. Li, *Angew. Chem. Int. Edit.*, 2021, **60**, 5708-5711.
24 D. Strmcnik, M. Uchimura, C. Wang, R. Subbaraman, N. Danilovic, D. van der Vliet, A. P. Paulikas, V. R. Stamenkovic and N. M. Markovic, *Nat. Chem.*, 2013, **5**, 300-306.
25 Y. Yang, X. D. Sun, G. Q. Han, X. Liu, X. Y. Zhang, Y. F. Sun, M. Zhang, Z. Cao and Y. J. Sun, *Angew. Chem. Int. Edit.*, 2019, **58**, 10644-10649.
26 Y. Qiu, L. Xin, Y. W. Li, I. T. McCrum, F. M. Guo, T. Ma, Y. Ren, Q. Liu, L. Zhou, S. Gu, M. J. Janik and W. Z. Li, *J. Am. Chem. Soc.*, 2018, **140**, 16580-16588.
27 F. L. Yang, X. Bao, P. Li, X. W. Wang, G. Z. Cheng, S. L. Chen and W. Luo, *Angew. Chem. Int. Edit.*, 2019, **58**, 14179-14183.
28 P. Sebastián-Pascual, Y. Shao-Horn and M. Escudero-Escribano, *Curr. Opin. Electrochem.*, 2022, **32**, 100918.

View Article Online
DOI: 10.1039/D4SC08259K

Chemical Science Accepted Manuscript

29 A. Montenegro, C. Dutta, M. Mammetkuliev, H. T. Shi, B. Y. Hou, D. Bhattacharyya, B. F. Zhao, S. B. Cronin and A. V. Benderskii, *Nature*, 2021, **594**, 62-65.
30 I. Ledezma-Yanez, W. D. Z. Wallace, P. Sebastian-Pascual, V. Climent, J. M. Feliu and M. T. M. Koper, *Nat. Energy*, 2017, **2**, 17031.
31 K. A. Sun, X. Y. Wu, Z. W. Zhuang, L. Y. Liu, J. J. Fang, L. Y. Zeng, J. G. Ma, S. J. Liu, J. Z. Li, R. Y. Dai, X. Tan, K. Yu, D. Liu, W. C. Cheong, A. J. Huang, Y. Q. Liu, Y. Pan, H. Xiao and C. Chen, *Nat. Commun.*, 2022, **13**, 6260.
32 M. G. Kim, S. H. Kim, J. H. Jang, D. W. Lee, D. Choi, J. H. Park, K. S. Lee, N. J. Chen, C. Hu, Y. M. Lee and S. J. Yoo, *Adv. Energy Mater.*, 2023, **13**, 2203133.
33 B. Mahler, V. Hoepfner, K. Liao and G. A. Ozin, *J. Am. Chem. Soc.*, 2014, **136**, 14121-14127.
34 M. F. Li, Z. P. Zhao, T. Cheng, A. Fortunelli, C. Y. Chen, R. Yu, Q. H. Zhang, L. Gu, B. V. Merinov, Z. Y. Lin, E. B. Zhu, T. Yu, Q. Y. Jia, J. H. Guo, L. Zhang, W. A. Goddard, Y. Huang and X. F. Duan, *Science*, 2016, **354**, 1414-1419.
35 R. Samanta, B. K. Manna, R. Trivedi, B. Chakraborty and S. Barman, *Chem. Sci.*, 2023, **15**, 364-378.
36 G. R. Xu, J. Bai, J. X. Jiang, J. M. Lee and Y. Chen, *Chem. Sci.*, 2017, **8**, 8411-8418.
37 Q. L. Wen, Y. Lin, Y. Yang, R. J. Gao, N. Q. Ouyang, D. F. Ding, Y. W. Liu and T. Y. Zhai, *ACS Nano*, 2022, **16**, 9572-9582.
38 Y. M. Shi, W. Du, W. Zhou, C. H. Wang, S. S. Lu, S. Y. Lu and B. Zhang, *Angew. Chem. Int. Edit.*, 2020, **59**, 22470-22474.
39 Y. Y. Cong, B. L. Yi and Y. J. Song, *Nano Energy*, 2018, **44**, 288-303.
40 C. Y. Yang, Y. B. Li, J. C. Yue, H. J. Cong and W. Luo, *Chem. Sci.*, 2023, **14**, 6289-6294.
41 X. Y. Tian, P. C. Zhao and W. C. Sheng, *Adv. Mater.*, 2019, **31**, 1808066.
42 H. S. Wang and H. D. Abruña, *J. Am. Chem. Soc.*, 2017, **139**, 6807-6810.
43 S. Q. Zhu, X. P. Qin, Y. Yao and M. H. Shao, *J. Am. Chem. Soc.*, 2020, **142**, 8748-8754.
44 M. Osawa, M. Tsushima, H. Mogami, G. Samjeské and A. Yamakata, *J. Phys. Chem. C*, 2008, **112**, 4248-4256.
45 L. F. Shen, B. A. Lu, Y. Y. Li, J. Liu, Z. C. Huang-fu, H. Peng, J. Y. Ye, X. M. Qu, J. M. Zhang, G. Li, W. B. Cai, Y. X. Jiang and S. G. Sun, *Angew. Chem. Int. Edit.*, 2020, **59**, 22397-22402.
46 M. M. Wang, K. A. Sun, W. L. Mi, C. Feng, Z. K. Guan, Y. Q. Liu and Y. Pan, *ACS Catal.*, 2022, **12**, 10771-10780.
47 J. Staszak-Jirkovsky, C. D. Malliakas, P. P. Lopes, N. Danilovic, S. S. Kota, K. C. Chang, B. Genorio, D. Strmcnik, V. R. Stamenkovic, M. G. Kanatzidis and N. M. Markovic, *Nat. Mater.*, 2016, **15**, 197-203.
48 M. Cabán-Acevedo, M. L. Stone, J. R. Schmidt, J. G. Thomas, Q. Ding, H. C. Chang, M. L. Tsai, J. H. He and S. Jin, *Nat. Mater.*, 2015, **14**, 1245-1251.
49 C. Y. Li, J. B. Le, Y. H. Wang, S. Chen, Z. L. Yang, J. F. Li, J. Cheng and Z. Q. Tian, *Nat. Mater.*, 2019, **18**, 697-701.
50 S. S. Li, L. Wu, Q. X. Liu, M. Y. Zhu, Z. H. Li, C. Wang, X. E. Jiang and J. H. Li, *J. Am. Chem. Soc.*, 2023, **145**, 26711-26719.
51 J. L. Bañuelos, E. Borguet, G. E. Brown, R. T. Cygan, J. J. DeYoreo, P. M. Dove, M. P. Gaigeot, F. M. Geiger, J. M. Gibbs, V. H. Grassian, A. G. Ilgen, Y. S. Jun, N. Kabengi, L. Katz, J. D. Kubicki, J. Lützenkirchen, C. V. Putnis, R. C. Remsing, K. M. Rosso, G. Rother, M. Sulpizi, M. Villalobos and H. C. Zhang, *Chem. Rev.*, 2023, **123**, 6413-6544.
52 J. B. Le, A. Cuesta and J. Cheng, *J. Electroanal. Chem.*, 2018, **819**, 87-94.
53 L. Li, Z. D. Wei, X. Q. Qi, M. T. Li, X. Huang, M. M. Deng and S. K. Jiang, *J. Phys. Chem. Lett.*, 2022, **13**, 10550-10557.
54 S. C. Zhu, R. O. Yang, H. J. W. Li, S. R. Huang, H. Z. Wang, Y. W. Liu, H. Q. Li and T. Y. Zhai, *Angew. Chem. Int. Edit.*, 2024, **63**, e202319462

55 Z. Y. Luo, L. Zhang, L. Wu, L. Wang, Q. L. Zhang, X. Z. Ren and X. L. Sun, *Nano Energy*, 2022, **102**, 107654.
56 D. Chen, R. H. Lu, R. H. Yu, Y. H. Dai, H. Y. Zhao, D. L. Wu, P. Y. Wang, J. W. Zhu, Z. H. Pu, L. Chen, J. Yu and S. C. Mu, *Angew. Chem.-Int. Edit.*, 2022, **61**, e202208642.
57 M. Luo, J. Y. Cai, J. S. Zou, Z. Jiang, G. M. Wang and X. W. Kang, *J. Mater. Chem. A*, 2021, **9**, 14941-14947.
58 E. Nikolla, J. Schwank and S. Linic, *J. Am. Chem. Soc.*, 2009, **131**, 2747-2754.
59 L. F. Shen, B. A. Lu, X. M. Qu, J. Y. Ye, J. M. Zhang, S. H. Yin, Q. H. Wu, R. X. Wang, S. Y. Shen, T. Sheng, Y. X. Jiang and S. G. Sun, *Nano Energy*, 2019, **62**, 601-609.
60 B. G. Mao, P. P. Sun, Y. Jiang, T. Meng, D. L. Guo, J. W. Qin and M. H. Cao, *Angew. Chem. Int. Edit.*, 2020, **59**, 15232-15237.
61 J. Deng, H. B. Li, S. H. Wang, D. Ding, M. S. Chen, C. Liu, Z. Q. Tian, K. S. Novoselov, C. Ma, D. H. Deng and X. H. Bao, *Nat. Commun.*, 2017, **8**, 14430.
62 F. L. Yang, P. Y. Han, N. Yao, G. Z. Cheng, S. L. Chen and W. Luo, *Chem. Sci.*, 2020, **11**, 12118-12123.

View Article Online
DOI: 10.1039/D4SC08139K

Chemical Science Accepted Manuscript

The data supporting this article have been included as part of the Supplementary Information.

Chemical Science Accepted Manuscript